

Boosting the intrinsic anomalous Hall effect through a topological phase transition in the magnetic Weyl semimetal $\text{Co}_3\text{Sn}_2\text{S}_2$

Hongyi Sun ^{1,2,3} and Qihang Liu^{1,4,*}

¹*Shenzhen Institute for Quantum Science and Engineering and Department of Physics, Southern University of Science and Technology, Shenzhen 518055, China*

²*International Quantum Academy, Shenzhen 518048, China*

³*Guangdong Provincial Key Laboratory of Quantum Science and Engineering, Southern University of Science and Technology, Shenzhen 518055, China*

⁴*Guangdong Provincial Key Laboratory of Computational Science and Material Design, Southern University of Science and Technology, Shenzhen 518055, China*



(Received 9 November 2022; revised 30 April 2023; accepted 12 May 2023; published 19 May 2023)

The anomalous Hall Effect (AHE) is one of the most fundamental phenomena related to band topology and holds great potential for technological applications. A promising approach to search for large AHE is to begin with a magnetic Weyl semimetal (WSM) and manipulate the Weyl nodes in the momentum-energy ($k-E$) space. However, controlling the Weyl points is generally difficult because Weyl nodes can robustly exist at a generic momentum. Here we realize this approach in an experimentally confirmed ferromagnetic WSM $\text{Co}_3\text{Sn}_2\text{S}_2$ via tension. Our calculations systematically demonstrate that the tension applied to $\text{Co}_3\text{Sn}_2\text{S}_2$ can drive the movement and annihilation of Weyl nodes in the $k-E$ space, triggering a high-Chern-number three-dimensional quantum AHE topological phase transition and thus greatly boosting the AHE. We also found a rare way of annihilation of Weyl nodes occurring near the Brillouin zone boundary. Our work offers a promising way to boost the AHE and sheds light on the search for three-dimensional quantum anomalous Hall insulators.

DOI: [10.1103/PhysRevB.107.205138](https://doi.org/10.1103/PhysRevB.107.205138)

I. INTRODUCTION

The anomalous Hall effect (AHE), where charge carriers acquire a transverse velocity component in the applied electric field without an external magnetic field, is one of the most intriguing and widely studied electronic transport phenomena [1]. The AHE has been proposed for its significant potential in various technical applications [2,3], such as highly sensitive sensors [4–7] and energy-efficient spintronic devices [8–10]. According to the current knowledge, there are two mechanisms accounting for the AHE: the extrinsic mechanism due to the scattering affected by the spin-orbit coupling (SOC) [11–13] and the intrinsic mechanism based on the Berry curvature framework [14–16], i.e.,

$$\sigma_{xy} = \frac{e^2}{\hbar} \frac{1}{N_k \Omega_c} \sum_k \sum_n f_{nk} \Omega_n^z(\mathbf{k}), \quad (1)$$

where σ_{xy} , N_k , Ω_c , f_{nk} , and $\Omega_n^z(\mathbf{k})$ are the Hall conductance, total number of k points in the Brillouin zone (BZ), volume of the primitive cell, Fermi distribution function, and Berry curvature, respectively [14]. The intrinsic mechanism can also explain the two-dimensional (2D) quantum anomalous Hall effect (QAHE), where all the valence bands are fully occupied in a gapped phase. The resultant anomalous Hall conductance (AHC) σ_{xy} is quantized to Ce^2/h (C is an integer and is known as the Chern number) accompanied with the presence of topological edge states [17,18].

Magnetic Weyl semimetals (WSMs) [19–22] host linear band intersections (Weyl points) around which the Berry curvature diverges, and hence are considered as a good platform for the AHE. Indeed, previous theoretical study has elaborated that the intrinsic AHC in magnetic WSMs with a single pair of Weyl nodes, when the Fermi level lies on the Weyl points, is proportional to $K_d \frac{e^2}{2\pi\hbar}$ (K_d is the momentum separation between Weyl nodes), thus providing a clear idea that the enhanced AHC can be acquired by manipulating the Weyl point in the BZ [23]. The discovery of various Weyl semimetals, such as $\text{Y}_2\text{Ir}_2\text{O}_7$ [19], HgCr_2Se_4 [24], $\text{Co}_3\text{Sn}_2\text{S}_2$ [25,26], and some Co-based Heusler compounds [27–30], has prompted considerable interest in studying the AHC on Weyl semimetals. In particular, $\text{Co}_3\text{Sn}_2\text{S}_2$ is a ferromagnetic (FM) WSM with three pairs of Weyl points near the Fermi energy, showing a large AHC of $-1130 \Omega^{-1} \text{cm}^{-1}$ [25,31]. Its AHC can be further exploited via chemical doping [32,33]. The AHC of some FM WSM Co-based Heusler compounds has the same magnitude as $\text{Co}_3\text{Sn}_2\text{S}_2$ [34,35] and can be tuned by an external magnetic field owing to their soft ferromagnetic properties [35]. On the other hand, it is challenging to further boost the intrinsic AHC of a WSM because the previous methods, such as disorder or doping, cannot effectively control the Weyl point evolution in the momentum space. Aside from the correlation with the AHE, the evolution of Weyl nodes is interesting for the topological phase transition accompanying the annihilation of Weyl nodes.

In this work, we enhance the AHE in FM WSM $\text{Co}_3\text{Sn}_2\text{S}_2$ by manipulating the Weyl points through tension (see Fig. 1). Since a Weyl node can robustly exist at a generic

*Corresponding author: liuqh@sustech.edu.cn

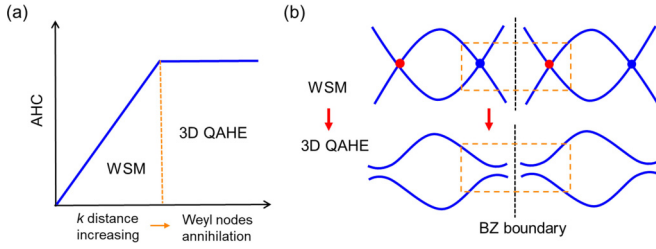


FIG. 1. Schematic diagram of boosting the intrinsic AHE through topological phase transition in magnetic Weyl semimetal. (a) AHE increases with the distance between Weyl nodes with different chirality and achieves its maximum value after a 3D QAHE phase transition accompanying the annihilation of Weyl nodes. Here, we assume the Weyl points are at the Fermi level. (b) Increasing the distance between Weyl points with different chirality in a BZ can lead to the annihilation of Weyl points with different chirality near the BZ boundary, causing a 3D QAHE insulator phase transition mentioned in (a). Red and blue points indicate Weyl nodes with positive and negative chirality, respectively.

momentum point without any crystal symmetry protection except for lattice translation, there are few reports on manipulating the Weyl points in the momentum space. Here, we report that the tension applied to WSM $\text{Co}_3\text{Sn}_2\text{S}_2$ can effectively drive the evolution and annihilation of the Weyl nodes, trigger a high-Chern-number three-dimensional (3D) QAHE topological phase transition, and greatly boost the AHE. In particular, the AHC can be doubled up to $-2200 \Omega^{-1} \text{cm}^{-1}$ by a 6% uniform tensile strain in the xy plane, and the induced general 3D QAHE phase hosts a high Chern number of -9 and correspondingly nine chiral surface sheet states. We also found a rare way of Weyl point annihilation that happened near the boundary of the BZ, which triggers the transition between different topological phases of matter.

II. COMPUTATIONAL METHODOLOGY

Density functional theory (DFT) calculations were performed using the projector-augmented wave (PAW) pseudopotentials with the exchange correlation of the Perdew-Burke-Ernzerhof revised for solids (PBEsol) form and the generalized gradient approximation (GGA) approach, as implemented in the Vienna *ab initio* Simulation Package (VASP) [36–38]. The cutoff energy for the plane-wave basis was set to 500 eV. The reciprocal space was sampled using a $15 \times 15 \times 15$ k mesh for structural optimization and self-consistent calculations. The equilibrium crystal lattice (a_0 , c_0) and atomic positions were fully relaxed until the atomic force on each atom was less than $10^{-2} \text{eV}/\text{\AA}$. The electronic structure of the equilibrium configuration was also verified by using the DS-PAW software [39]. For each stretched structure, the atomic force was relaxed using fixed lattice constants. We constructed maximally localized Wannier representations [40] by projecting the Bloch states (with an $11 \times 11 \times 11$ k mesh) from the DFT calculations of bulk materials onto Co-3*d*, S-3*p*, Sn-5*s*, and Sn-5*p* orbitals. The AHC is expressed as the sum of the Berry curvature over all the occupied states, as shown in Eq. (1). We define the band-occupied AHC as $\sigma_{xy}^{\text{band}} = \frac{e^2}{h} \frac{1}{N_k \Omega_c} \sum_{\mathbf{k}} \sum_n \Omega_n^z(\mathbf{k})$, where

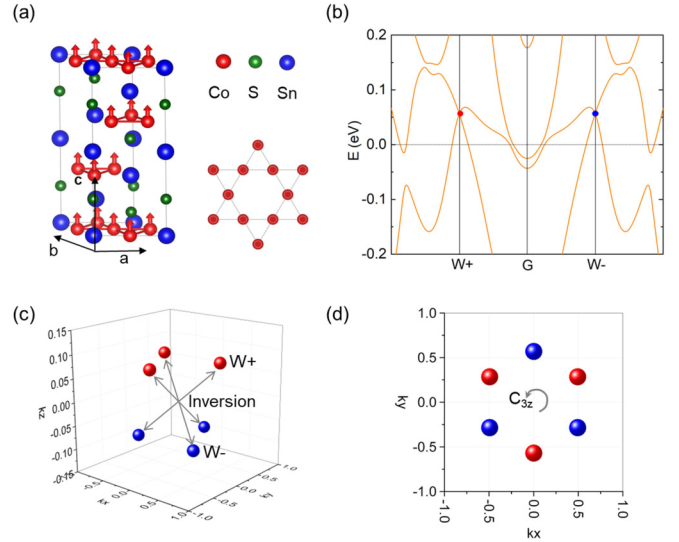


FIG. 2. Crystal and band structure of primitive $\text{Co}_3\text{Sn}_2\text{S}_2$. (a) $\text{Co}_3\text{Sn}_2\text{S}_2$ unit cell in hexagonal setting (left) and the kagome plane formed by Co atoms (right). The Co atoms are magnetized along the z (c) direction. (b) Band structure along a path connecting a pair of Weyl points. (c),(d) Six Weyl nodes linked by C_{3z} and space inversion symmetries. Red and blue points indicate Weyl nodes with different chirality.

n is the band index and $1 \leq n \leq$ the number of valence electrons. The locations and chirality of the Weyl nodes, AHC, band-occupied AHC (with a $200 \times 200 \times 200$ k mesh), Chern number, and chiral edge states were calculated in the tight-binding models constructed by these Wannier representations, as implemented in the WANNIERTOOLS package [41].

III. RESULTS AND DISCUSSION

A. Electronic structure of equilibrium configuration

$\text{Co}_3\text{Sn}_2\text{S}_2$ crystallizes in a rhombohedral structure with the space group $R\bar{3}m$ (no. 166) [42]. As shown in Fig. 2(a), the Co atoms form quasi-2D kagome planes and magnetize along the z (c) direction in a hexagonal unit cell. The Curie temperature is 177 K and the local magnetic moment is $0.33\mu_B$ per Co atom. The optimized lattice constants for the equilibrium configuration are $a_0 = 5.295 \text{\AA}$ and $c_0 = 12.984 \text{\AA}$. Our calculated magnetic moment and lattice constants are very close to the experimental values [25,43].

As an FM WSM, $\text{Co}_3\text{Sn}_2\text{S}_2$ hosts three pairs of Weyl nodes (approximately 60 meV above the Fermi level) in the BZ, as shown in Figs. 2(b) and 2(c). The C_{3z} and space inversion symmetries in $\text{Co}_3\text{Sn}_2\text{S}_2$ map one Weyl node to the other five nodes. As a result, the six Weyl nodes share the same energy [Fig. 2(b)] and are distributed on two parallel planes along the z direction on which the Weyl nodes have opposite chirality [Figs. 2(c) and 2(d)]. For convenience, we denote these two planes as PW+ and PW−, respectively. Additionally, the C_{3z} constrains the AHC tensor to $\sigma_{xz} = \sigma_{zx} = \sigma_{yz} = \sigma_{zy} = 0$ and $\sigma_{xy} = -\sigma_{yx}$. The surviving σ_{xy} is from the contribution of $\Omega_n^z(\mathbf{k})$, as shown in Eq. (1). To investigate σ_{xy} , we calculated the Chern numbers of various planes along the z direction [i.e., the flux of $\Omega_n^z(\mathbf{k})$], except for PW+ and PW−,

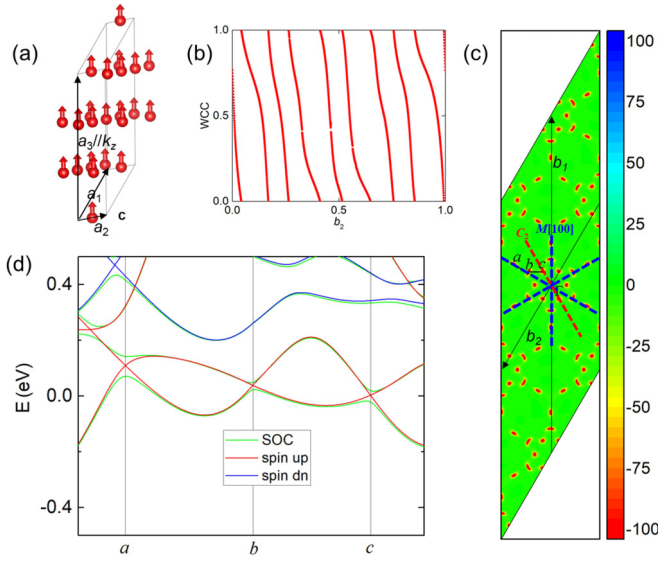


FIG. 3. The origin of the Chern number -9 . (a) The specially designed primitive cell for the calculation of Chern number. Only the magnetic Co atoms and the crystal lattice are shown. (b) The evolution of Wannier charge center (WCC) on the $k_z = 0$ plane, indicating the Chern number $C = -9$. (c) The Berry curvature of the valence band on the $k_z = 0$ plane in the 2×2 BZ. The black solid, blue dashed, and red dashed lines represent the BZ boundaries, three mirrors and a C_2 axis, respectively. (d) The band structures with and without SOC along path a - b - c as shown in (c).

because the Chern number can only be defined for planes in the BZ without band crossings. Interestingly, we find the Chern number $C = -9$ for all planes between PW+ and PW-, and $C = -6$ for other planes. The difference between the Chern numbers of the planes on either side of the Weyl point is equal to the sum of the chirality of the sandwiched Weyl points, consistent with the statement that the Weyl node can be viewed as the source or drain of the Berry curvature. The proximity of Weyl nodes to the Fermi level and the high Chern number on the xy plane in BZ are responsible for the large AHE of $-1105 \Omega^{-1} \text{cm}^{-1}$ in primitive $\text{Co}_3\text{Sn}_2\text{S}_2$, which agrees with previous findings [25,31].

We now discuss the origin of the high Chern number $C = -9$ on the k_z planes between PW+ and PW-. To calculate the Chern number, we used a specially designed primitive cell as depicted in Fig. 3(a). In this cell, the lattice basis vector \mathbf{a}_3 is parallel to the magnetic moment of Co atoms and aligned with the z direction of the Cartesian coordinate system. In this case, due to the relationship between the reciprocal lattice basis vectors (\mathbf{b}_1 , \mathbf{b}_2 , \mathbf{b}_3) and the lattice basis vectors (\mathbf{a}_1 , \mathbf{a}_2 , \mathbf{a}_3), the planes parallel to the b_1b_2 plane are also parallel to the xy plane. The Chern numbers of these planes between PW+ and PW- are the same since there is no energy gap closing. Thus, we can select the $k_z = 0$ plane for our analysis. Our Wannier charge center (WCC) calculation indicates $C = -9$ for this plane [Fig. 3(b)]. Additionally, we calculated the Berry curvature on this plane to identify the origin of the Chern number. As shown in Fig. 3(c), there are 18 regions with large Berry curvature on the $k_z = 0$ plane in a BZ (a total of 72 regions on the $k_z = 0$ plane in the

2×2 BZ), and each region has the same sign of the Berry curvature. These features suggest the existence of 18 band inversion points. When SOC is not considered, the $k_z = 0$ plane has mirror symmetry M [100], C_{3z} symmetry, and space inversion symmetry [Fig. 3(c)]. From these three points, a , b , and c , the other 15 points in a BZ can be obtained through the above symmetry operations [Fig. 3(c)]. Therefore, only these three points a , b , and c need to be examined. When SOC is not considered, the energy bands cross near the points, a , b , and c , to form three Dirac points [Fig. 3(d)]. The band degeneracy at points a and b is protected by the mirror symmetry, while that at point c is protected by the C_2 axis passing through point c on the $k_z = 0$ plane (C_2 is the joint operation of mirror symmetry and space inversion) [Fig. 3(c)]. When SOC is included, the mirror symmetry is broken, and so are the symmetries protecting the degeneracy of points a , b , and c , leading to energy gaps at these three points [Fig. 3(d)]. Since each gapped Dirac point can contribute a AHC of $-0.5 e^2/h$ [44,45], and there are 18 such points on the $k_z = 0$ plane in a BZ, the total AHC is $-9 e^2/h$ and the corresponding $C = -9$. We also confirmed that the sum of the contributions of other occupied energy bands (except the bands forming the gapped Dirac points) to the AHC is zero, further showing that the Chern number of -9 arises from the 18 gapped Dirac cones.

B. Weyl nodes evolution and enhanced anomalous Hall effect

The idea for enhancing the intrinsic AHE based on magnetic WMS is to make the Weyl points closer to the Fermi level while increasing the separation between Weyl points with opposite chirality, as shown in Fig. 1(a). In principle, a Weyl node can robustly exist at a generic momentum, and there is no general method to control the Weyl points in the momentum space. However, considering that strain can affect electron hopping and thus bandwidth, the Weyl points (band crossings) may be driven by strain to move in the momentum space. We applied different uniform tensions in the xy plane and z direction (denoted as S_{ij} , where i and j are the stretch rates in the xy plane and z directions, respectively) to track the motions of the Weyl points in the momentum space. The stretched structures maintained the same symmetry as the original equilibrium one. As mentioned above, the six Weyl points in $\text{Co}_3\text{Sn}_2\text{S}_2$ share the same energy and can be linked by C_{3z} and spatial inversion symmetries, therefore, it is sufficient to track the evolution of a single Weyl point. Figures 4(a) and 4(b) show the evolution of the Weyl points with tensile strain in the energy and momentum spaces, respectively. We found that the tension in the xy plane (z direction) moves the Weyl point closer to (away from) the Fermi level [Fig. 4(a)], and the tensions in both directions increase the separation of Weyl points with different chirality, i.e., the separation between PW+ and PW- [Figs. 4(b) and 4(c)]. The positions of the Weyl nodes relative to the Fermi level and the separation of the Weyl points of different chirality jointly determine the AHE. We found that tensions along the z direction will reduce the AHC, while tensions in the xy plane can significantly enhance the AHC, as shown in Figs. 4(b) and 4(d). In particular, a 6% tensile strain in the xy plane (S_{60}) will double the AHC of $\text{Co}_3\text{Sn}_2\text{S}_2$ up to $-2200 \Omega^{-1} \text{cm}^{-1}$. Interestingly, we found

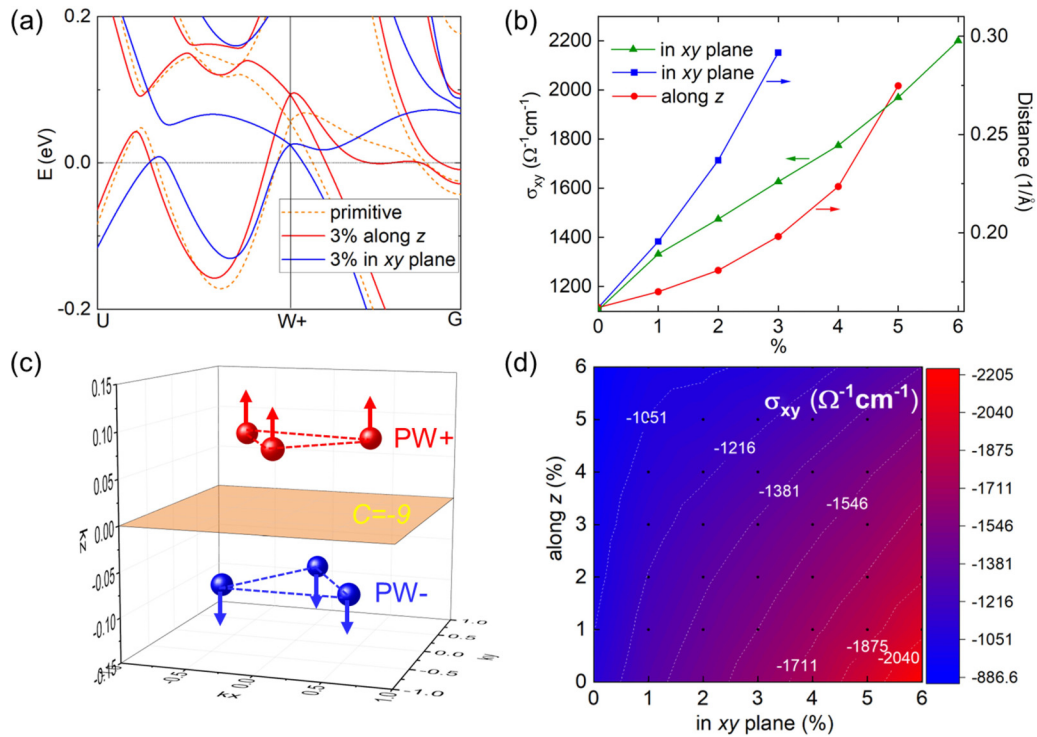


FIG. 4. Weyl nodes evolution and enhanced AHE. (a) Evolution of Weyl nodes in the energy space. “W+” represents three different positions of the selected Weyl point in three stretch cases, aligned on the band path for the convenience of drawing without affecting the discussion. “%” represents the stretch rate (the same below). (b) The tension-enhanced AHC and the enlarged z direction separation of the Weyl points with different chirality in moment space, i.e., the separation between planes of $PW+$ and $PW-$ shown in (c). (d) Interpolated stretch-dependent AHC contour map. The black dots in the figure represent the calculated configurations. The AHC can be doubled up to $-2200 \Omega^{-1} \text{cm}^{-1}$ by a 6% tensile strain in xy plane.

that the Weyl nodes are all annihilated in the configuration S_{60} , and a band structure with direct band gaps appears, implying a topological phase transition. Previous theories have predicted that the annihilation of Weyl nodes can drive the system to a trivial insulator, an axion insulator, or a 3D QAHE state, depending on the energy gap property [46,47]. The appearance of the topological phase without Weyl points, yet with the AHE, suggests that it is neither a trivial insulator nor an axion insulator. We discuss this topological phase and the annihilation of Weyl nodes in detail below.

C. Annihilation of Weyl nodes and topological phase transition

When Weyl points with different chirality meet at a k point, they will annihilate each other and a topological phase transition will appear. Recently, the annihilation of Weyl points has attracted considerable attention. The conventional thought is that the Weyl points move, meet, and annihilate within the BZ. Recent studies reported that the annihilation of Weyl nodes can also occur between different spin channels, i.e., the Weyl points formed by two energy bands of one spin channel are annihilated by those formed by two other bands of the other spin channel [48,49]. This annihilation is accompanied by the degeneration of two spin channels, i.e., a magnetic phase transition. To investigate the annihilation of Weyl nodes, we calculated 49 stretched configurations to track the evolution of the band structure. We found that tensions in the xy plane and z direction can both cause band inversion at

the inversion-invariant moment point L ($0, 0, 1/2$) [Fig. 5(a)]. This band inversion can be indicated by the parity of the states at the L point because our stretched structures maintain spatial inversion symmetry. As shown in Fig. 5(b), as the stretching increases, the Weyl point $W_{13}+$ with positive chirality near the L point in configuration S_{13} evolves to $W_{14}+$ in configuration S_{14} . At the same time, configuration S_{14} creates a new Weyl point $W'_{14}-$ with negative chirality near the L point owing to the energy band inversion. The Weyl points $W_{14}+$ and $W'_{14}-$ meet and annihilate each other in a more stretched configuration S_{15} , resulting in a band structure with direct gaps. This annihilation of the Weyl point, different from most reported previously, occurs near the BZ boundary: the six old Weyl points evolve to the vicinity of the BZ and are annihilated by the six newly generated Weyl points owing to the band inversion at the BZ boundary.

The “insulator” phase that emerges after the annihilation of all Weyl nodes can be topologically categorized, despite the absence of a global band gap, yet possessing direct band gaps. For this, we calculated the symmetry indicator of space inversion symmetry $Z_4 : (Z_2, Z_2, Z_2)$ [50–52] based on the parities of eight inversion-invariant momenta in the BZ for all our 49 stretched structures. Owing to the C_{3z} symmetry, a total of three band inversions at L and its two other equivalent points are present near the phase-transition critical point, as shown in Table I. The calculated symmetry indicator divides the 49 stretched structures into three groups, including the WMS phase 3 : ($0, 0, 0$) with three pairs of Weyl nodes,

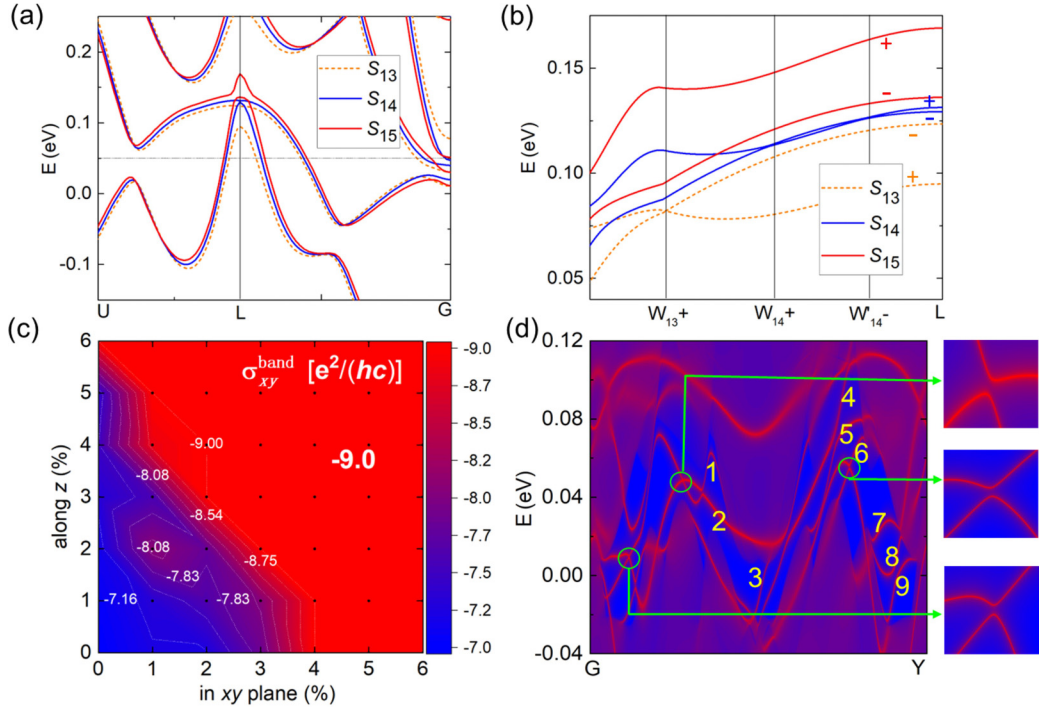


FIG. 5. Annihilation of Weyl nodes and topological phase transition. (a) Tension induces a band inversion at L ($0, 0, 1/2$), implying a topological phase transition. S_{ij} denotes the stretched crystal structure with stretch rates i and j in the xy plane and z direction, respectively. (b) Band inversion at L leads to the creation and annihilation of Weyl points. The band path passes through the Weyl nodes W_{13+} in configuration S_{13} , the W_{14+} and the newly created W'_{14-} in configuration S_{14} . “+” and “-” represent the parity of the quantum state at L point. (c) Interpolated stretch-dependent band-occupied AHC contour map in unit of $e^2/(hc)$, where c is the lattice constant along z direction in the hexagonal setting. The band-occupied AHC is quantized to $-9 e^2/(hc)$ in the red region, indicating a 3D QAHE phase. The black dots in the figure represent the calculated configurations. “%” represents the stretch rate. (d) Nine chiral surface sheet states on the (010) surface arise in the 3D QAHE phase in configuration S_{44} . The blue region indicates the direct band gaps between quantum states far away from the surface.

WSM phase 2 : (1, 1, 1) with six pairs of Weyl nodes, and 3D QAHE phase 2 : (1, 1, 1). The WSM phase with six pairs of Weyl nodes exists in our configuration S_{14} . There is a clear boundary between the WMS and 3D QAHE phases, as shown in Fig. 5(c).

We now discuss the 3D QAHE phase induced by the annihilation of the Weyl points in detail. The 3D QAHE phase can be regarded as a stack of series of imaginary 2D QAHE insulators (with the same Chern number) along the FM direction in the BZ [53,54]. For this reason, the 3D QAHE can be expressed using Eq. (1) as

$$\sigma_{xy}^{\text{3D QAHE}} = C \frac{e^2}{hc}, \quad (2)$$

TABLE I. Parity-based symmetry indicator $Z_4 : (Z_2, Z_2, Z_2)$. A topological phase transition from WSM phase 3 : (0, 0, 0) to the 3D QAHE phase 2 : (1, 1, 1). n_{occ}^- indicates the number of the occupied bands with odd parity at eight time-reversal-invariant momenta points and $Z_4 = \sum_K n_{\text{occ}}^- \bmod 4$, $Z_{2,i} = \sum_{K_i=\pi} n_{\text{occ}}^- \bmod 2$, where K represents all the inversion-invariant momenta [50–52].

Γ_i	$G(0,0,0)$	$3L(0,0,1/2)$	$3F(1/2,1/2,0)$	$T(1/2,1/2,1/2)$	$Z_4 : (Z_2, Z_2, Z_2)$
n_{occ}^-	14	36	27	24	3 : (0, 0, 0)
n_{occ}^-	14	37	27	24	2 : (1, 1, 1)

where C is the Chern number of these “imaginary 2D QAHE insulators” and c is the real-space periodic length along the FM direction (i.e., lattice constant). Equation (2) was introduced in the study of the 3D quantum Hall effect (QHE) of a 3D electron gas system under strong magnetic fields [55,56]. The 3D QHE requires stringent conditions and has been pursued for 30 years. Until recently, the 3D QHE was only observed in Cd_3As_2 [57,58] and ZrTe_5 [59,60] owing to complicated mechanisms such as the Weyl orbit and charge density wave. On the other hand, the 3D QAHE insulator can enable the quantization of AHC owing to its intrinsic topological nontrivial bulk gap. To date, few 3D QAHE insulators have been theoretically proposed, such as LaCl and LaBr [61], $\text{Ba}_2\text{Cr}_7\text{O}_{14}$, and $h\text{-Fe}_3\text{O}_4$ [62], but not yet been confirmed

experimentally. Alternatively, we demonstrate in this study that, based on the well-studied Weyl semimetal $\text{Co}_3\text{Sn}_2\text{S}_2$, the 3D QAHE phase may be obtained through a topological phase transition, as shown in Table I.

To further confirm the 3D QAHE phase predicted by the symmetry indicator in Table I, we calculated the band-occupied AHC and the surface states of the surface parallel to the z direction in the 3D QAHE phase, as shown in Figs. 5(c) and 5(d), respectively. The band-occupied AHC is defined as $\sigma_{xy}^{\text{band}} = \frac{e^2}{h} \frac{1}{N_k \Omega_c} \sum_{\mathbf{k}} \sum_n \Omega_n^z(\mathbf{k})$, where n is the band index. As shown in Fig. 5(c), the calculated band-occupied AHC is clearly quantized to $-9 e^2/(hc)$ for all the 3D QAHE phases predicted by the symmetry indicator, where c is the lattice constant along the z direction in a hexagonal setting. The number “-9” is exactly the Chern number of the planes between $\text{PW}+$ and $\text{PW}-$, as shown in Fig. 4(c). As the tension increased, the distance between $\text{PW}+$ and $\text{PW}-$ gradually increased and spanned the entire BZ after the 3D QAHE topological transition, resulting in a stack of a series of imaginary 2D QAHE insulators with a high Chern number of -9, i.e., the 3D QAHE of $-9 e^2/(hc)$.

In addition, we calculated the local density of states on the (010) surface of configuration S_{44} (in a hexagonal unit cell setting), as shown in Fig. 5(d). As expected, the existence of nine chiral surface sheet states perfectly agreed with the topological prediction by the Chern number of -9 in the xy plane. It should be noted that the chiral surface states in Fig. 5(d) are buried in the bulk metallic states at G and Y , where the conduction and valence bands are generally indistinguishable. These bulk metallic states are caused by the BZ folding of the bulk states that host direct band gaps but not a global one. Even so, after careful identification, one can still distinguish nine chiral surface sheet states connecting the “conduction” and “valence” bands, as shown in Fig. 5(d).

IV. DISCUSSION AND CONCLUSION

The key to achieving the large AHE is the large Berry curvature in the BZ; it is a good option to enhance the AHE based on well-studied magnetic WSM materials, such as $\text{Co}_3\text{Sn}_2\text{S}_2$, because of the large Berry curvature inherent in them. The idea of using a magnetic WSM to boost the AHE is relatively clear, i.e., to increase the spacing between the Weyl points with different chirality and to make the Weyl points closer to the Fermi level. The difficulty lies in effectively moving the Weyl points to achieve the above purposes. The application of strain can alter the electron hopping, influencing the energy band width and hence modifying the Weyl point.

We note that several studies have investigated the effects of the compressive strain on the AHE of $\text{Co}_3\text{Sn}_2\text{S}_2$. When subjected to increasing pressure, it was observed that both the AHE and ferromagnetism became gradually suppressed, and ultimately vanished at higher pressure [63,64]. The reduction in AHE was attributed to the decrement of the effective distance between Weyl points with opposite chirality. Additionally, the magnetic correlations in $\text{Co}_3\text{Sn}_2\text{S}_2$ were explored, revealing that while the sample exhibits an out-of-plane ferromagnetic ground state, an in-plane antiferromagnetic state appears at temperatures above 90 K, and

the increased pressure or temperature can suppress the out-of-plane ferromagnetic ground state and thereby reduce the AHE [65]. Furthermore, the In doping can tune the competition between FM, xy -plane AFM and mostly xy -plane helimagnetic orders in $\text{Co}_3\text{Sn}_{2-x}\text{In}_x\text{S}_2$, and the AHE can be driven nonmonotonically due to several possible reasons [66]. It was also shown that the pressure can reduce the effective distance between Weyl points with opposite chirality and thus reduce the AHE. The system evolves into a general Z_2 topological insulator phase with time-reversal symmetry at 40.4 GPa, where the AHE vanishes and the original Weyl points are annihilated by the new ones from the other spin channel [49]. In short, the previous studies all suggest that pressure reduces the out-of-plane ferromagnetism, the effective distance between Weyl points with different chirality, and thus the intrinsic AHE in $\text{Co}_3\text{Sn}_2\text{S}_2$. In contrast, as demonstrated in this work, tensile strain in $\text{Co}_3\text{Sn}_2\text{S}_2$ can enhance the spacing between the Weyl points with different chirality and bring the Weyl points closer to the Fermi level, thereby enhancing the intrinsic AHC monotonically. Experimentally, obtaining large nonuniform stretches, such as a 6% xy -plane tensile strain, is challenging. Nevertheless, our results indicate that the intrinsic AHE in $\text{Co}_3\text{Sn}_2\text{S}_2$ can monotonically and significantly increase over a broad xy -plane tensile strain range 0–6% [Fig. 4(b)], which may be applied through substrates with different lattice constants.

Achieving a 3D QAHE phase from the magnetic Weyl phase is more challenging than enhancing the AHE. Necessary conditions for such a transformation include moving the Weyl points, annihilating them, and generating a nontrivial energy gap, ideally a global nontrivial energy gap. Moreover, the magnetic WSM phase may not necessarily evolve into a 3D QAHE phase, and instead, it could become an axion insulator or a trivial insulator, depending on the band evolution and energy gap property [46,47]. For example, if the band inversion in Table I occurred not at L (0, 0, 1/2) and its two equivalent points, but at the G point (0, 0, 0) ($n_{\text{occ}}^- = 15$), the gapped phase can be a trivial insulator with the symmetry indicator $Z_4 : (Z_2, Z_2, Z_2) = 0 : (0, 0, 0)$. If the band inversion occurred at $3F$ (1/2, 1/2, 0) points ($n_{\text{occ}}^- = 28$), the gapped phase can be an axion insulator with the symmetry indicator $Z_4 : (Z_2, Z_2, Z_2) = 2 : (0, 0, 0)$. Our results showed that $\text{Co}_3\text{Sn}_2\text{S}_2$ could successfully enter the 3D QAHE phase over a relatively broad tensile strain range. Although a global energy gap is not further realized, it can serve as a demonstration that a magnetic WSM can transit into the 3D QAHE phase accompanying Weyl point annihilation near the BZ boundary which has also been reported in ZrTe_5 [67]. Additionally, and more importantly, even without a global energy gap, the appearance of the 3D QAHE phase can significantly enhance the AHE by a fine-tuned chemical potential.

In summary, we proposed that tension applied to FM WSM $\text{Co}_3\text{Sn}_2\text{S}_2$ can effectively modulate the Weyl nodes, induce a general 3D QAHE phase accompanying Weyl point annihilation, and enhance the intrinsic AHE over a broad tensile strain range. The tension in the xy plane (z direction) moves the Weyl point closer to (away from) the Fermi level and increases the separation of Weyl points with different chirality. As the applied tension increases, the original three pairs of

Weyl points in $\text{Co}_3\text{Sn}_2\text{S}_2$ annihilated with the newly generated ones, leading to a general 3D QAHE phase with a quantized high AHC of $-9e^2/(hc)$. The annihilation of Weyl nodes occurs near the BZ boundary. The general 3D QAHE phase is confirmed by our analysis and computations of the parity, symmetry indicator, xy -plane Chern number, quantized 3D AHC, and chiral surface states. The AHE can be modulated in the range -886 to $-2200 \Omega^{-1} \text{cm}^{-1}$ (i.e., 20% reduction to 100% enhancement) by uniform tensile strains of 0–6% in the xy plane and z direction. Therefore, our work provides a promising approach to enhance the AHE and sheds light on the search for 3D QAHE phases.

ACKNOWLEDGMENTS

This work was supported by National Key R&D Program of China under Grant No. 2020YFA0308900, Guangdong Innovative and Entrepreneurial Research Team Program under Grant No. 2017ZT07C062, Guangdong Provincial Key Laboratory for Computational Science and Material Design under Grant No. 2019B030301001, the Shenzhen Science and Technology Program (Grant No. KQTD20190929173815000) and Center for Computational Science and Engineering of Southern University of Science and Technology. We also gratefully acknowledge HZWTECH for providing computation facilities.

-
- [1] N. Nagaosa, J. Sinova, S. Onoda, A. H. MacDonald, and N. P. Ong, Anomalous Hall effect, *Rev. Mod. Phys.* **82**, 1539 (2010).
- [2] C. M. Hurd, *The Hall Effect in Metals and Alloys* (Plenum, New York, 1972).
- [3] C. L. Chien and C. R. Westgate, *The Hall Effect and its Applications* (Plenum, New York, 1972).
- [4] Y. Zhang, Q. Hao, and G. Xiao, Low-frequency noise of magnetic sensors based on the anomalous Hall effect in Fe–Pt alloys, *Sensors* **19**, 3537 (2019).
- [5] J. Moritz, B. Rodmacq, S. Auffret, and B. Dieny, Extraordinary Hall effect in thin magnetic films and its potential for sensors, memories and magnetic logic applications, *J. Phys. D: Appl. Phys.* **41**, 135001 (2008).
- [6] Y. M. Lu, J. W. Cai, H. Y. Pan, and L. Sun, Ultrasensitive anomalous Hall effect in $\text{SiO}_2/\text{Fe-Pt}/\text{SiO}_2$ sandwich structure films, *Appl. Phys. Lett.* **100**, 022404 (2012).
- [7] K. Wang, Y. Zhang, and G. Xiao, Anomalous Hall Sensors with High Sensitivity and Stability Based on Interlayer Exchange-Coupled Magnetic Thin Films, *Phys. Rev. Appl.* **13**, 064009 (2020).
- [8] S. Iihama, T. Taniguchi, K. Yakushiji, A. Fukushima, Y. Shiota, S. Tsunegi, R. Hiramatsu, S. Yuasa, Y. Suzuki, and H. Kubota, Spin-transfer torque induced by the spin anomalous Hall effect, *Nat. Electron.* **1**, 120 (2018).
- [9] J. Puebla, J. Kim, K. Kondou, and Y. Otani, Spintronic devices for energy-efficient data storage and energy harvesting, *Commun. Mater.* **1**, 24 (2020).
- [10] M. Dc, R. Grassi, J.-Y. Chen, M. Jamali, D. Reifsnnyder Hickey, D. Zhang, Z. Zhao, H. Li, P. Quarterman, Y. Lv *et al.*, Room-temperature high spin–orbit torque due to quantum confinement in sputtered $\text{BixSe}(1-x)$ films, *Nat. Mater.* **17**, 800 (2018).
- [11] L. Berger, Side-jump mechanism for the Hall effect of ferromagnets, *Phys. Rev. B* **2**, 4559 (1970).
- [12] J. Smit, The spontaneous Hall effect in ferromagnetics I, *Physica* **21**, 877 (1955).
- [13] J. Smit, The spontaneous Hall effect in ferromagnetics II, *Physica* **24**, 39 (1958).
- [14] D. Xiao, M.-C. Chang, and Q. Niu, Berry phase effects on electronic properties, *Rev. Mod. Phys.* **82**, 1959 (2010).
- [15] M. Onoda and N. Nagaosa, Quantized Anomalous Hall Effect in Two-Dimensional Ferromagnets: Quantum Hall Effect in Metals, *Phys. Rev. Lett.* **90**, 206601 (2003).
- [16] F. D. M. Haldane, Berry Curvature on the Fermi Surface: Anomalous Hall Effect as a Topological Fermi-Liquid Property, *Phys. Rev. Lett.* **93**, 206602 (2004).
- [17] C.-X. Liu, S.-C. Zhang, and X.-L. Qi, The quantum anomalous Hall effect: Theory and experiment, *Annu. Rev. Condens. Matter Phys.* **7**, 301 (2016).
- [18] D. J. Thouless, M. Kohmoto, M. P. Nightingale, and M. den Nijs, Quantized Hall Conductance in a Two-Dimensional Periodic Potential, *Phys. Rev. Lett.* **49**, 405 (1982).
- [19] X. Wan, A. M. Turner, A. Vishwanath, and S. Y. Savrasov, Topological semimetal and Fermi-arc surface states in the electronic structure of pyrochlore iridates, *Phys. Rev. B* **83**, 205101 (2011).
- [20] A. A. Burkov, M. D. Hook, and L. Balents, Topological nodal semimetals, *Phys. Rev. B* **84**, 235126 (2011).
- [21] B. Yan and C. Felser, Topological materials: Weyl semimetals, *Annu. Rev. Condens. Matter Phys.* **8**, 337 (2017).
- [22] N. P. Armitage, E. J. Mele, and A. Vishwanath, Weyl and Dirac semimetals in three-dimensional solids, *Rev. Mod. Phys.* **90**, 015001 (2018).
- [23] A. A. Burkov, Anomalous Hall Effect in Weyl Metals, *Phys. Rev. Lett.* **113**, 187202 (2014).
- [24] G. Xu, H. Weng, Z. Wang, X. Dai, and Z. Fang, Chern Semimetal and the Quantized Anomalous Hall Effect in HgCr_2Se_4 , *Phys. Rev. Lett.* **107**, 186806 (2011).
- [25] E. Liu, Y. Sun, N. Kumar, L. Muechler, A. Sun, L. Jiao, S.-Y. Yang, D. Liu, A. Liang, Q. Xu *et al.*, Giant anomalous Hall effect in a ferromagnetic kagome-lattice semimetal, *Nat. Phys.* **14**, 1125 (2018).
- [26] N. Morali, R. Batabyal, P. K. Nag, E. Liu, Q. Xu, Y. Sun, B. Yan, C. Felser, N. Avraham, and H. Beidenkopf, Fermi-arc diversity on surface terminations of the magnetic Weyl semimetal $\text{Co}_3\text{Sn}_2\text{S}_2$, *Science* **365**, 1286 (2019).
- [27] J. Kübler and C. Felser, Weyl points in the ferromagnetic Heusler compound Co_2MnAl , *Europhys. Lett.* **114**, 47005 (2016).
- [28] Z. Wang, M. G. Vergniory, S. Kushwaha, M. Hirschberger, E. V. Chulkov, A. Ernst, N. P. Ong, R. J. Cava, and B. A. Bernevig, Time-Reversal-Breaking Weyl Fermions in Magnetic Heusler Alloys, *Phys. Rev. Lett.* **117**, 236401 (2016).
- [29] G. Chang, S.-Y. Xu, H. Zheng, B. Singh, C.-H. Hsu, G. Bian, N. Alidoust, I. Belopolski, D. S. Sanchez, S. Zhang *et al.*, Room-temperature magnetic topological Weyl fermion and nodal line

- semimetal states in half-metallic Heusler Co_2TiX ($X = \text{Si, Ge, or Sn}$), *Sci. Rep.* **6**, 38839 (2016).
- [30] I. Belopolski, K. Manna, D. S. Sanchez, G. Chang, B. Ernst, J. Yin, S. S. Zhang, T. Cochran, N. Shumiya, H. Zheng *et al.*, Discovery of topological Weyl fermion lines and drum-head surface states in a room temperature magnet, *Science* **365**, 1278 (2019).
- [31] Q. Wang, Y. Xu, R. Lou, Z. Liu, M. Li, Y. Huang, D. Shen, H. Weng, S. Wang, and H. Lei, Large intrinsic anomalous Hall effect in half-metallic ferromagnet $\text{Co}_3\text{Sn}_2\text{S}_2$ with magnetic Weyl fermions, *Nat. Commun.* **9**, 3681 (2018).
- [32] J. Shen, Q. Yao, Q. Zeng, H. Sun, X. Xi, G. Wu, W. Wang, B. Shen, Q. Liu, and E. Liu, Local Disorder-Induced Elevation of Intrinsic Anomalous Hall Conductance in an Electron-Doped Magnetic Weyl Semimetal, *Phys. Rev. Lett.* **125**, 086602 (2020).
- [33] J. Shen, Q. Zeng, S. Zhang, H. Sun, Q. Yao, X. Xi, W. Wang, G. Wu, B. Shen, Q. Liu *et al.*, 33% Giant anomalous Hall current driven by both intrinsic and extrinsic contributions in magnetic weyl semimetal $\text{Co}_3\text{Sn}_2\text{S}_2$, *Adv. Funct. Mater.* **30**, 2000830 (2020).
- [34] A. Sakai, Y. P. Mizuta, A. A. Nugroho, R. Sihombing, T. Koretsune, M.-T. Suzuki, N. Takemori, R. Ishii, D. Nishio-Hamane, R. Arita *et al.*, Giant anomalous Nernst effect and quantum-critical scaling in a ferromagnetic semimetal, *Nat. Phys.* **14**, 1119 (2018).
- [35] P. Li, J. Koo, W. Ning, J. Li, L. Miao, L. Min, Y. Zhu, Y. Wang, N. Alem, C.-X. Liu *et al.*, Giant room temperature anomalous Hall effect and tunable topology in a ferromagnetic topological semimetal Co_2MnAl , *Nat. Commun.* **11**, 3476 (2020).
- [36] G. Kresse and J. Furthmüller, Efficient iterative schemes for ab initio total-energy calculations using a plane-wave basis set, *Phys. Rev. B* **54**, 11169 (1996).
- [37] J. P. Perdew, A. Ruzsinszky, G. I. Csonka, O. A. Vydrov, G. E. Scuseria, L. A. Constantin, X. Zhou, and K. Burke, Restoring the Density-Gradient Expansion for Exchange in Solids and Surfaces, *Phys. Rev. Lett.* **100**, 136406 (2008).
- [38] G. Kresse and D. Joubert, From ultrasoft pseudopotentials to the projector augmented-wave method, *Phys. Rev. B* **59**, 1758 (1999).
- [39] P. E. Blöchl, Projector augmented-wave method, *Phys. Rev. B* **50**, 17953 (1994).
- [40] A. A. Mostofi, J. R. Yates, Y.-S. Lee, I. Souza, D. Vanderbilt, and N. Marzari, Wannier90: A tool for obtaining maximally-localised Wannier functions, *Comput. Phys. Commun.* **178**, 685 (2008).
- [41] Q. Wu, S. Zhang, H.-F. Song, M. Troyer, and A. A. Soluyanov, WannierTools: An open-source software package for novel topological materials, *Comput. Phys. Commun.* **224**, 405 (2018).
- [42] R. Wehrich, I. Anusca, and M. Zabel, Half-antiperovskites: Structure and type-antitype relations of shandites $\text{M}_{3/2}\text{AS}$ ($M = \text{Co, Ni}$; $A = \text{In, Sn}$), *Z. Anorg. Allg. Chem.* **631**, 1463 (2005).
- [43] P. Vaqueiro and G. G. Sobany, A powder neutron diffraction study of the metallic ferromagnet $\text{Co}_3\text{Sn}_2\text{S}_2$, *Solid State Sci.* **11**, 513 (2009).
- [44] B. A. Bernevig, *Topological Insulators and Topological Superconductors* (Princeton University Press, Princeton, 2013).
- [45] Z. Li, Y. Han, and Z. Qiao, Chern Number Tunable Quantum Anomalous Hall Effect in Monolayer Transitional Metal Oxides via Manipulating Magnetization Orientation, *Phys. Rev. Lett.* **129**, 036801 (2022).
- [46] A. A. Burkov and L. Balents, Weyl Semimetal in a Topological Insulator Multilayer, *Phys. Rev. Lett.* **107**, 127205 (2011).
- [47] M. Gu, J. Li, H. Sun, Y. Zhao, C. Liu, J. Liu, H. Lu, and Q. Liu, Spectral signatures of the surface anomalous Hall effect in magnetic axion insulators, *Nat. Commun.* **12**, 3524 (2021).
- [48] I. Belopolski, T. A. Cochran, X. Liu, Z.-J. Cheng, X. P. Yang, Z. Guguchia, S. S. Tsirkin, J.-X. Yin, P. Vir, G. S. Thakur *et al.*, Signatures of Weyl Fermion Annihilation in a Correlated Kagome Magnet, *Phys. Rev. Lett.* **127**, 256403 (2021).
- [49] Q. Zeng, H. Sun, J. Shen, Q. Yao, Q. Zhang, N. Li, L. Jiao, H. Wei, C. Felser, Y. Wang *et al.*, Pressure-Driven Magneto-Topological Phase Transition in a Magnetic Weyl Semimetal, *Adv. Quantum Technol.* **5**, 2100149 (2022).
- [50] J. Kruthoff, J. de Boer, J. van Wezel, C. L. Kane, and R.-J. Slager, Topological Classification of Crystalline Insulators through Band Structure Combinatorics, *Phys. Rev. X* **7**, 041069 (2017).
- [51] H. Watanabe, C. Po Hoi, and A. Vishwanath, Structure and topology of band structures in the 1651 magnetic space groups, *Sci. Adv.* **4**, eaat8685 (2018).
- [52] S. Ono and H. Watanabe, Unified understanding of symmetry indicators for all internal symmetry classes, *Phys. Rev. B* **98**, 115150 (2018).
- [53] T. L. Hughes, E. Prodan, and B. A. Bernevig, Inversion-symmetric topological insulators, *Phys. Rev. B* **83**, 245132 (2011).
- [54] D. Gresch, G. Autès, O. V. Yazyev, M. Troyer, D. Vanderbilt, B. A. Bernevig, and A. A. Soluyanov, Z2Pack: Numerical implementation of hybrid Wannier centers for identifying topological materials, *Phys. Rev. B* **95**, 075146 (2017).
- [55] B. I. Halperin, Possible states for a three-dimensional electron gas in a strong magnetic field, *Jpn. J. Appl. Phys.* **26**, 1913 (1987).
- [56] M. Kohmoto, B. I. Halperin, and Y.-S. Wu, Diophantine equation for the three-dimensional quantum Hall effect, *Phys. Rev. B* **45**, 13488 (1992).
- [57] C. M. Wang, H.-P. Sun, H.-Z. Lu, and X. C. Xie, 3D Quantum Hall Effect of Fermi Arcs in Topological Semimetals, *Phys. Rev. Lett.* **119**, 136806 (2017).
- [58] C. Zhang, Y. Zhang, X. Yuan, S. Lu, J. Zhang, A. Narayan, Y. Liu, H. Zhang, Z. Ni, R. Liu *et al.*, Quantum Hall effect based on Weyl orbits in Cd_3As_2 , *Nature (London)* **565**, 331 (2019).
- [59] F. Tang, Y. Ren, P. Wang, R. Zhong, J. Schneeloch, S. A. Yang, K. Yang, P. A. Lee, G. Gu, Z. Qiao *et al.*, Three-dimensional quantum Hall effect and metal-insulator transition in ZrTe_5 , *Nature (London)* **569**, 537 (2019).
- [60] F. Qin, S. Li, Z. Z. Du, C. M. Wang, W. Zhang, D. Yu, H.-Z. Lu, and X. C. Xie, Theory for the Charge-Density-Wave Mechanism of 3D Quantum Hall Effect, *Phys. Rev. Lett.* **125**, 206601 (2020).
- [61] M. Wu, High-temperature intrinsic quantum anomalous Hall effect in rare Earth monohalide, *2D Mater.* **4**, 021014 (2017).
- [62] Y. J. Jin, R. Wang, B. W. Xia, B. B. Zheng, and H. Xu, Three-dimensional quantum anomalous Hall effect in ferromagnetic insulators, *Phys. Rev. B* **98**, 081101(R) (2018).

- [63] Z. Y. Liu, T. Zhang, S. X. Xu, P. T. Yang, Q. Wang, H. C. Lei, Y. Sui, Y. Uwatoko, B. S. Wang, H. M. Weng *et al.*, Pressure effect on the anomalous Hall effect of ferromagnetic Weyl semimetal $\text{Co}_3\text{Sn}_2\text{S}_2$, *Phys. Rev. Mater.* **4**, 044203 (2020).
- [64] X. Chen, M. Wang, C. Gu, S. Wang, Y. Zhou, C. An, Y. Zhou, B. Zhang, C. Chen, Y. Yuan *et al.*, Pressure-tunable large anomalous Hall effect of the ferromagnetic kagome-lattice Weyl semimetal $\text{Co}_3\text{Sn}_2\text{S}_2$, *Phys. Rev. B* **100**, 165145 (2019).
- [65] Z. Guguchia, J. A. T. Verezhak, D. J. Gawryluk, S. S. Tsirkin, J. X. Yin, I. Belopolski, H. Zhou, G. Simutis, S. S. Zhang, T. A. Cochran *et al.*, Tunable anomalous Hall conductivity through volume-wise magnetic competition in a topological kagome magnet, *Nat. Commun.* **11**, 559 (2020).
- [66] Z. Guguchia, H. Zhou, C. N. Wang, J. X. Yin, C. Mielke, S. S. Tsirkin, I. Belopolski, S. S. Zhang, T. A. Cochran, T. Neupert *et al.*, Multiple quantum phase transitions of different nature in the topological kagome magnet $\text{Co}_3\text{Sn}_{2-x}\text{In}_x\text{S}_2$, *npj Quantum Mater.* **6**, 50 (2021).
- [67] G. Zheng, X. Zhu, Y. Liu, J. Lu, W. Ning, H. Zhang, W. Gao, Y. Han, J. Yang, H. Du *et al.*, Field-induced topological phase transition from a three-dimensional Weyl semimetal to a two-dimensional massive Dirac metal in ZrTe_5 , *Phys. Rev. B* **96**, 121401(R) (2017).